Journal of The Electrochemical Society, **152** (3) C116-C123 (2005)
0013-4651/2005/152(3)/C116/8/$7.00 © The Electrochemical Society, Inc.

In Situ Stress Measurements during Copper Electrodeposition on (111)-Textured Au

O. E. Kongstein, U. Bertocci,* and G. R. Stafford*,z

Materials Science and Engineering Laboratory, National Institute of Standards and Technology, Gaithersburg, Maryland 20899, USA

In situ stress measurements were made during copper electrodeposition onto (111)-textured Au from acidic sulfate electrolyte using the wafer curvature method. In the Cu underpotential deposition region, the intermediate $(\sqrt{3} \times \sqrt{3})$R30° Cu-sulfate honeycomb structure creates a surface stress that is tensile when compared to that of the sulfate-adsorbed electrode at positive potentials or the complete (1×1) Cu monolayer at more negative potentials. This behavior is consistent with surface-induced charge redistribution models that appear in the literature. During the bulk deposition of Cu, there is a rapid increase in tensile stress during the first 20 nm of growth that we attribute to nuclei coalescence and grain boundary formation. The magnitude of the tensile stress as well as the film thickness at which the maximum stress occurs are both dependent upon the electrode potential due to its influence on the nucleation density. When the films are continuous, the total stress is the superposition of the coalescence-induced tensile stress and a compressive stress which we attribute to the incorporation of mobile adatoms on the surface into the grain boundaries. The tensile stress component dominates thin films deposited at high overpotential, whereas thick films deposited at low overpotential have a net compressive stress. When deposition is interrupted both tensile and compressive components of the stress relax somewhat but are quickly reestablished when deposition is resumed. The development of the growth stress that we describe here is very similar to that which has been reported for Cu deposition from the vapor phase.
 [DOI: 10.1149/1.1854093]

Manuscript submitted April 28, 2004; revised manuscript received July 29, 2004. Available electronically January 24, 2005.

Electrodeposition is used by the microelectronics community to produce solderable surface finishes, magnetic recording media, and copper interconnections in printed circuit boards and integrated circuits. These films tend to develop sizable mechanical stresses as a result of the nucleation and growth process or from the use of solution additives and alloying elements needed to achieve desired deposition rates and mechanical properties. Often, these stresses can approach or exceed the yield stress of the bulk material and can lead to loss of adhesion and the generation of bulk and surface defects. As the feature sizes in microelectronic components continue to shrink, the stresses associated with the earliest stages of film growth raise serious concerns in the industry about device performance and reliability.

The stress observed at room temperature on a coated surface is typically the result of two different phenomena. The first, thermal stress, is present when the film is deposited at a temperature different from the service temperature and the film and substrate have different thermal expansion coefficients. The second, intrinsic stress, is caused by the manner in which the film grows and can arise from lattice-mismatched epitaxial growth, nuclei coalescence and grain growth during deposition, incorporation of impurities or side-reaction products, and phase transformations accompanied by volume changes. Although similar growth morphologies and stress development are inherent to both electrodeposited films[1] and those grown from the gas phase, the latter community has placed more effort in understanding the microstructural contributions to film stress.

The growth stresses associated with Volmer-Weber growth from the gas-phase have been divided into three distinct modes;[2-6] low-mobility columnar growth, epitaxial growth, and high-mobility island growth. The low-mobility columnar films develop tensile stresses, epitaxial Volmer-Weber films are completely compressive, while high-mobility films are initially tensile but become compressive as the film thickens. The general observation in the latter case is that the stress progresses from compressive to tensile and then back to compressive. This has been referred to as CTC behavior. The initial compressive stress occurs in the discrete-nuclei stage of growth and is due to the surface stress of these small particles. The rapid development of tensile stress is associated with nuclei coalescence and grain boundary formation while the final compressive stage occurs during thickening of the continuous film.

The electrodeposition community has been keenly interested in residual stress and its measurement. Several techniques have been developed, most of which are outlined in a series of review papers by Weil.[1,7,8] The simplest and most widely used methods involve the measurement of the deflection of a flexible cathode, typically in a direction that is perpendicular to the in-plane stress generated in the film. Fairly sophisticated methods for tracking this deflection have been developed in the last 15 years, the more popular make use of interferometry,[9,10] capacitance measurements,[11] laser beam reflection,[12-16] and scanning tunneling microscopy (STM) and atomic force microscopy (AFM).[17-19] These *in situ* stress measurements have been used to examine adsorbate-induced surface stress,[10,11,16,18,20-23] underpotential deposition,[17,19,24-26] electrochemical insertion and intercalation reactions,[12,13,15,27] and bulk film deposition.[9,28,29]

Haiss *et al.* have examined the stress evolution during the first 25 monolayers of copper electrodeposition onto Au(111).[29] Using an STM to monitor wafer deflection, they were able to observe the surface stresses associated with sulfate ion desorption as well as copper underpotential deposition (upd), three-dimensional nucleation, and growth. Bulk copper films developed tensile stresses, the magnitude of which was dependent on the deposition potential. Their observations were consistent with stress development as the result of nuclei coalescence and grain boundary formation. Qualitatively, the growth behavior of Cu on Au(111) was similar to low-mobility Volmer-Weber growth observed in gas-phase deposition.[2,3] Although this growth mode is generally seen in high melting point metals, it was postulated that sulfate adsorption may reduce ad-atom surface mobility sufficiently so that a low-mobility growth mode is operative.

In situ stress measurements during the vapor deposition of copper show that the growth stress follows CTC behavior with the final tensile-compressive transition occurring when the film thickness exceeds 10 nm.[4] Because the stress data of Haiss *et al.*[29] on electrodeposited Cu is limited to films less than 7 nm thick, the missing tensile-compressive transition may be due to insufficient film thickness rather than limited ad-atom surface mobility. The purpose of this paper is to examine the stresses associated with the earliest stages of copper deposition from sulfate electrolyte and to extend the work of Haiss by examining films up to 400 nm in thickness.

* Electrochemical Society Active Member.
z E-mail: gery.stafford@nist.gov

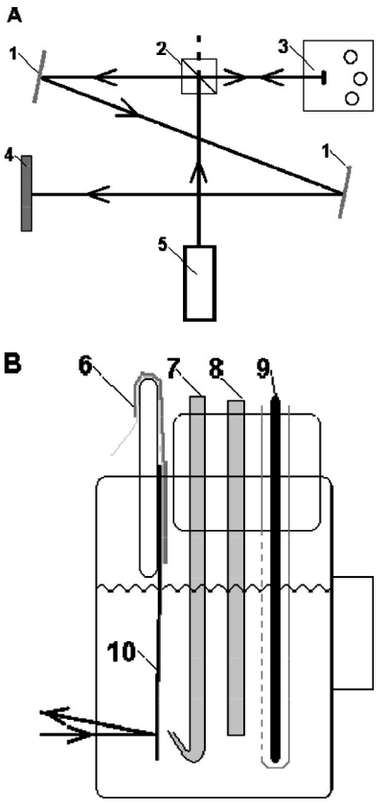

Figure 1. (a) The laser path: 1-mirror, 2-beam splitter, 3-electrochemical cell, 4-position sensing detector, 5-laser; (b) the electrochemical cell, 6-tape and copper foil, 7-capillary for the reference electrode, 8-nitrogen inlet, 9-counter electrode, 10-cantilever working electrode.

Experimental

A schematic of the components of the *in situ* stress measurement apparatus is shown in Fig. 1. The light source was a 1 mW Helium-Neon laser (JDS[a] Uniphase, model 1108P). A beam splitter was placed in the path of the beam so that the incident and reflected beams were coincident. Two mirrors were placed in the path of the reflected laser beam in order to increase the optical lever. A duo-lateral position sensitive detector (PSD) with dimensions 20×20 mm (DLS-20 from UTD Sensors Inc.) was used to measure the position of the reflected beam. The four voltages from the PSD were amplified, measured by a National Instrument A/D card, and then transferred to a Macintosh Power PC computer. They were then converted into vertical and horizontal positions on the PSD. The stress calculation utilized only the vertical position of the laser.

The cantilever was a borosilicate glass slide (D 263, Schott) measuring $60 \times 3 \times 0.108$ mm. The glass had a Young's Modulus of $72.9 \cdot 10^9$ N m^{-2} and a Poisson ratio of 0.208, as specified by the vendor. To one side of this substrate a 4 nm thick adhesion layer of titanium and a 250 nm film of gold were vapor-deposited. This glass-metal interface provided the reflective surface for the laser beam. Prior to use, the electrodes were boiled in distilled water and then held in a hydrogen flame for ~1 s. These Au electrodes had a strong (111) crystallographic orientation. The 200 reflection was not apparent in θ-2θ X-ray scans and rocking curves of the 111 reflection generally yielded a full-width half-maximum (FWHM) on the order of 2°.

The electrochemical cell was a single compartment Pyrex cell. A glass disc was joined to the back of the cell to allow the cell to be held and positioned by a standard mirror mount on the optical bench. A glass plate was vertically joined to the top of the cell to support the top of the cantilever working electrode. A piece of 0.025 mm thick copper foil was placed over the cantilever in order to make electrical contact to the gold prior to taping the cantilever to the glass plate support. The electrolyte used in this study was 0.1 mol L^{-1} H_2SO_4 (Environmental Grade Plus, Alfa Aesar) +10 mmol L^{-1} $CuSO_4$ (Mallinckrodt). The distilled water was further purified using an EASY pure UV ultrapure water system (Barnstead). Prior to making a measurement, the electrolyte was purged with nitrogen. A nitrogen purge above the electrolyte was continued during a measurement. The reference electrode was a saturated calomel electrode (SCE). To avoid contamination of potassium chloride from the SCE and minimize the IR-drop between the reference and working electrode a salt bridge and capillary were used. Potential control was maintained using an EG&G Princeton Applied Research Corp. (PARC) model 273 potentiostat/galvanostat that was controlled by a Macintosh Power PC computer and LabView software.

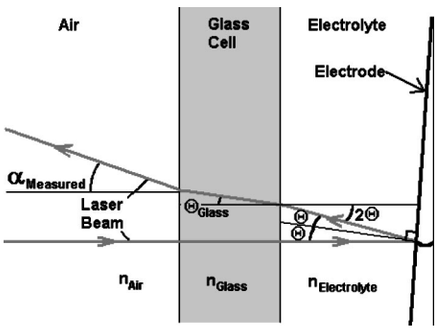

Figure 2. The laser beam path through the electrochemical cell.

In an effort to obtain reproducible current and stress transients, an electrochemical pretreatment was performed. Prior to examining the upd of Cu on (111)-textured Au, the electrode potential was swept approximately 10 times between 1.5 and 0.015 V at a sweep rate of 0.050 V s^{-1}. Prior to each bulk deposition experiment the electrode potential was sequentially stepped to −0.70 V for 2 s, to +0.065 V for 10 s, and to +1.4 V for 10 s. This procedure was repeated four times before adjusting the potential to +0.30 V for 1 min. The potential was then stepped to the desired deposition potential for a pre-determined film thickness while the cantilever deflection was monitored by the PSD. Following deposition, the Cu was electrochemically stripped from the cantilever. In all cases reported here, the electrochemical charge measured during Cu deposition and dissolution was equal and the cantilever returned to its original position indicating that alloying with the Au substrate was minimal.

The in-plane stress developed in the electrodeposited film creates curvature in the cantilever. Since the electrodeposit is on the side away from the laser, compressive stress in the film displaces the cantilever towards the laser while a tensile stress displaces the cantilever away from the laser. Figure 2 shows the geometric relationships between the deflected cantilever and the reflected laser beam. The radius of curvature of the cantilever is given by

$$R = \frac{L}{\Theta} \qquad [1]$$

where L is the length of electrode submerged into the electrolyte down to where the laser strikes the electrode and Θ is the angle of deflection. When no electrolyte is present in the cell, the angle of the reflected beam α_{meas} is simply equal to 2Θ. However, when the cell is filled with electrolyte, a correction must be made to account for the difference in the refractive index between the electrolyte inside the cell and the air outside the cell. According to Snell's Law[14]

[a] Certain trade names are mentioned for experimental information only, in no case does it imply a recommendation or endorsement by NIST.

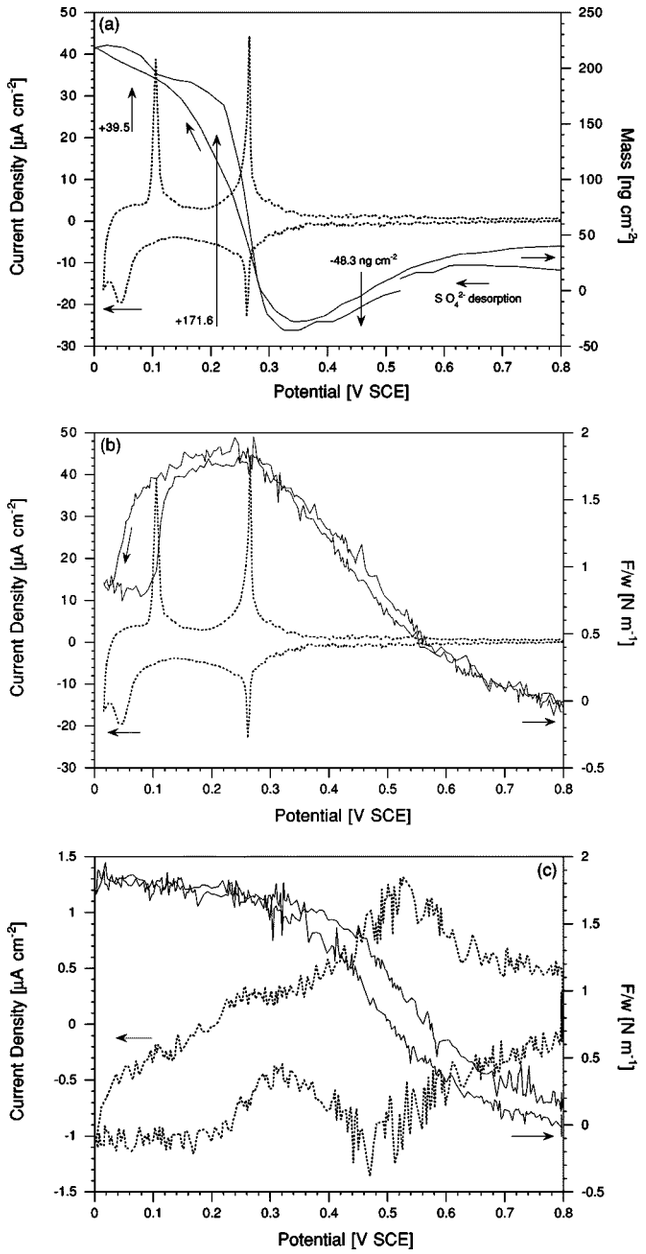

Figure 3. (a) Linear sweep voltammetry and EQCM response associated with the underpotential deposition of Cu onto (111)-textured Au; (b) linear sweep voltammetry and surface stress associated with the underpotential deposition of Cu onto (111)-textured Au; (c) linear sweep voltammetry and surface stress when $CuSO_4$ is not present.

$$n_{air}\alpha_{meas} = n_{H_2O}2\Theta \qquad [2]$$

where n_{air} is the refractive index of air ($n_{air} = 1.0$) and n_{H_2O} is the refractive index of the electrolyte ($n_{H_2O} = 1.33$). The radius of curvature of the cantilever in terms of the measured angle of reflection of the laser becomes

$$R = \frac{2Ln_{H_2O}}{n_{air}\alpha_{meas}} \qquad [3]$$

The relationship between the force (F) per cantilever beam width (w) exerted by the electrodeposit and the radius of curvature of the cantilever is given by Stoney's equation[30]

$$F(t_f)/w = \frac{E_s \cdot t_s^2}{6(1-\nu_s)R} = \int_0^{t_f}\sigma(t)dt \qquad [4]$$

where E_s, ν_s, and t_s are the Young's modulus, Poisson ratio, and thickness of the glass substrate respectively, and R is the radius of curvature of the cantilever. The force on the cantilever, F/w, is the integral of the film stress, $\sigma(t)$, and is a function of the film thickness, t_f, at any given time. This simplified version of Stoney's equation requires only the elastic properties of the substrate. The properties of the electrodeposit can be ignored if the deposit thickness is less than 5% of the substrate thickness.[31] We have thus limited our experiments to deposit thicknesses less than 5 μm. Combining Eq. 3 and 4 yields Stoney's equation in terms of the laser reflection angle, and assuming that $\tan(\alpha_{meas}) \approx \alpha_{meas} = d_{psd}/D_{psd}$, in terms of the PSD output

$$F/w = \frac{E_s \cdot t_s^2 n_{air}\alpha_{meas}}{6(1-\nu_s)2Ln_{H_2O}} = \frac{E_s \cdot t_s^2 n_{air}d_{psd}}{6(1-\nu_s)2Ln_{H_2O}D_{psd}} \qquad [5]$$

where d_{psd} is the vertical coordinate of the reflected laser beam onto the PSD and D_{psd} is the distance of the PSD from the electrode. For a given substrate, the sensitivity of the measurement is limited by the resolution of the PSD but can be improved by using long electrodes (L) and by increasing the distance between the PSD and the electrode (D_{psd}). D_{psd} was accurately measured by tilting the cell through a series of known angles using a micrometer and was determined from the slope of the d_{psd} *vs.* Θ_{meas} plot. A typical value of D_{psd} was 2.075 m. Because the maximum cantilever deflection is on the order of a few μm, we ignore its influence on D_{psd}. The parameter L was also determined by adjusting the height of the cell using a z-stage micrometer while monitoring changes in the PSD signal intensity. Based on a PSD resolution of 4 μm and a typical optical bench geometry, a theoretical limit to the F/w resolution is 0.004 N m^{-1}. Experimentally we have determined the resolution to be about 0.03 N m^{-1} with the electrode in solution.

The cantilever deflection data is presented in three ways; the F/w is determined from d_{psd} (Eq. 5), the average film stress, σ_{avg}, is the F/w divided by the film thickness, and the incremental film stress, $\sigma(t)$, is the slope of the F/w-thickness curve. The latter two are defined as

$$\sigma_{avg} = \frac{F/w}{t_f}, \quad \sigma(t) = \frac{d(F/w)}{dt} \qquad [6]$$

In determining the incremental stress, each F/w-thickness curve was fit to a sixth order polynomial and then differentiated with respect to the thickness. The deposit thickness was calculated from the deposition charge, assuming a bulk density for Cu and a 100% current efficiency for the copper deposition reaction.

The electrochemical quartz microbalance (EQMB) measurements of Cu upd on Au were made on 5 MHz polished quartz crystals, on which Au was vapor deposited onto a Ti bonding layer. Prior to use, the Au vapor deposit was examined by X-ray diffraction (XRD) and crystals with strong (111) texture were selected for the measurements. The measuring instrument recorded the resonant frequency as well as the resistance of the quartz crystal equivalent circuit. This value is related to the mechanical losses in the resonant circuit, mainly due to the roughness of the metal-electrolyte interface. In surface adsorption or upd, surface roughness is not affected. The resistance measurements served only to ensure that unexpected surface changes did not occur. The EQMB data were acquired, at intervals of the order of 1 s, while a potentiostat, under computer control, applied preselected programs to the Au electrode. As refer-

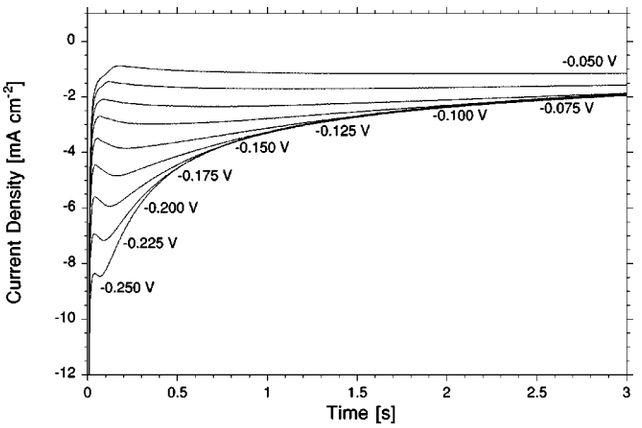

Figure 4. Chronoamperograms for Cu deposition onto (111)-textured Au in 0.1 mol L^{-1} H_2SO_4 + 10 mmol L^{-1} $CuSO_4$. The potential was stepped from +0.3 V to a deposition potential ranging from −0.05 to −0.25 V in 0.025 V increments.

ence electrode, either Cu or a saturated Hg sulfate electrode (SSE) was used; however, all electrode potential values are given with respect to SCE.

Results

Cu UPD.—The underpotential deposition of copper onto Au(111) in the presence of sulfate has been extensively examined by *ex situ* UHV techniques,[32-34] as well as *in situ* techniques such as surface extended X-ray absorption fine structure (EXAFS),[35-37] STM,[38,39] AFM,[40] infrared spectroscopy,[41] X-ray scattering,[42,43] quartz crystal microgravimetry,[44-46] and a variety of electrochemical techniques.[47-50] At potentials approaching 1.0 V *vs.* SCE, adsorbed sulfate ions form an ordered $(\sqrt{3} \times \sqrt{7})$ structure (0.218 coverage of the Au(111) surface).[51,52] As the potential is decreased towards the potential of zero charge (pzc) for Au(111) in sulfate (0.35 V), the coverage of the adsorbed sulfate decreases to near zero. The upd of Cu in the presence of sulfate occurs in two distinct electrochemical steps, see Fig. 3a voltammetry. The first Cu adsorption step at 0.26 V can be ascribed to a $(\sqrt{3} \times \sqrt{3})$R30° honeycomb superstructure where sulfate occupies one of the three-fold sites and copper occupies the two remaining three-fold sites. Copper adsorption promotes the adsorption of sulfate which in turn stabilizes the sub-monolayer copper structure. The second Cu upd wave occurs at +0.06 V and represents the formation of a complete Cu monolayer which is in registry with the substrate (1 × 1 structure). Because Cu has a more negative pzc than Au, the sulfate re-adsorbs onto the Cu surface with similar coverage (about 20%).

Our results in the Cu upd region are shown in Fig. 3. The total charge recorded for the two upd steps is 475 μC cm^{-2} which is close to the 445 μC cm^{-2} expected for a $2e^-$ reduction of Cu^{2+} per Au atom on the Au(111) surface. When the upd layer was electrochemically removed, the Au was exactly the same as before the upd, suggesting that the upd is completely reversible and that no alloying occurs. Figure 3a also shows the quartz crystal microbalance response in the Cu upd region. In the SO_4^{2-} desorption region between 0.8 and 0.35 V, a weight loss of 50 to 60 ng cm^{-2} is measured. This is very close to the theoretical value of 48.3 ng cm^{-2} for the complete desorption of $(\sqrt{3} \times \sqrt{7})$ sulfate from Au(111). An increase of about 200 ng cm^{-2} is measured for the first Cu upd step which is slightly higher than the expected 171.6 ng cm^{-2} for the formation of the Cu-sulfate honeycomb structure. Finally, a gain of 39.5 ng cm^{-2} is expected for completion of the Cu monolayer and readsorption of the sulfate onto the copper surface, very similar to what is observed experimentally. Our EQCM response is very similar to that reported by Borges *et al.*[45]

Figure 3b shows the surface stress associated with the Cu-sulfate upd process which is very similar to that reported by Haiss for this system.[17,24] As the potential of the Au electrode is swept cathodically from +0.8 V, the surface stress increases approximately 1.8 N m^{-1} and reaches a maximum following the first upd wave. This change in the surface stress in the tensile direction is associated with the removal of the sulfate adlayer from the Au surface. The formation of the $(\sqrt{3} \times \sqrt{3})$R30° sulfate-copper honeycomb structure has little impact on the surface stress as the surface stress remains at 1.8 N m^{-1} (as shown in Fig. 3c) whether Cu^{2+} is present in the electrolyte or not. The completion of the Cu monolayer, which includes the readsorption of sulfate onto the Cu surface, causes a 1 N m^{-1} compressive shift in the surface stress. The surface stress essentially re-traces itself, taking into account the irreversibility of the more cathodic upd wave, when the potential sweep is reversed and the Cu upd layer is anodically stripped from the Au surface.

A simple surface-induced charge redistribution model has been used to explain the stress behavior in the upd region. Ibach[11,21] has suggested that the loss of bonds at a clean metal surface causes an increased charge density between the remaining surface atoms, thereby increasing their attractive interaction and resulting in a tensile stress at the surface. This tensile stress, which has been estimated to be 2.7 N m^{-1} for Au(111),[53] has been observed in most free-electron metals and is a likely driving force for surface reconstruction.[23] The adsorption of species on the surface can also be expected to alter the surface stress because the local interaction of each adsorbate will alter the bond strength between neighboring atoms on the surface. Electron donors would be expected to cause tensile stress as they increase the bond charge density between the underlying metal atoms whereas electron acceptors such as adsorbed anions cause compressive stress because they reduce the electron density in the surface. In the present case, the coadsorption of Cu and sulfate in the $(\sqrt{3} \times \sqrt{3})$R30° honeycomb configuration appears to have little interaction with the increased charge density at the Au surface. The adsorption of sulfate at more positive potentials causes a decrease in the tensile stress which is consistent with the charge-induced surface stress model described above. On the cathodic side of the honeycomb structure the monolayer of Cu is not expected to generate a misfit stress since Cu is 11.4% smaller than Au and easily fits into the threefold site. However, because the pzc for Cu in sulfate is about 0.8 V negative of the Au pzc,[54] the Cu overlayer results in the accumulation of positive charge on the metal surface and a relaxation in the charge-induced tensile stress at the surface. Another way of looking at this is that the negative shift of the pzc with the completion of the Cu monolayer leads to sulfate adsorption on the Cu surface and a relaxation of the tensile stress, similar to that observed for sulfate on Au at anodic potentials. We have measured the sulfate desorption from Cu(111) to occur at about −0.5 V in this electrolyte.

Bulk Cu deposition.—The bulk deposition of Cu was examined by pulsing the potential of the Au cantilever electrode from an initial potential of +0.3 V to a variety of deposition potentials, ranging from −0.050 to −0.250 V. The chronoamperograms are shown in Fig. 4. These transients are consistent with a three-dimensional nucleation process and at deposition potentials more negative than −0.1 V, the growth is diffusion controlled; *i.e.*, the current transient follows the diffusion-limited Cottrell current. Normalization of these current transients in the traditional way[55] indicates that the nucleation is instantaneous although the nucleation behavior can be influenced by electrode pre-treatment.

Figure 5 shows the force per cantilever beam width, F/w, the average film stress, σ_{avg}, and the incremental film stress, $\sigma(t)$, plotted as a function of deposit thickness. Because the initial electrode potential is +0.3 V, the sulfate is desorbed prior to initiating the deposition. After applying the appropriate deposition potential, the

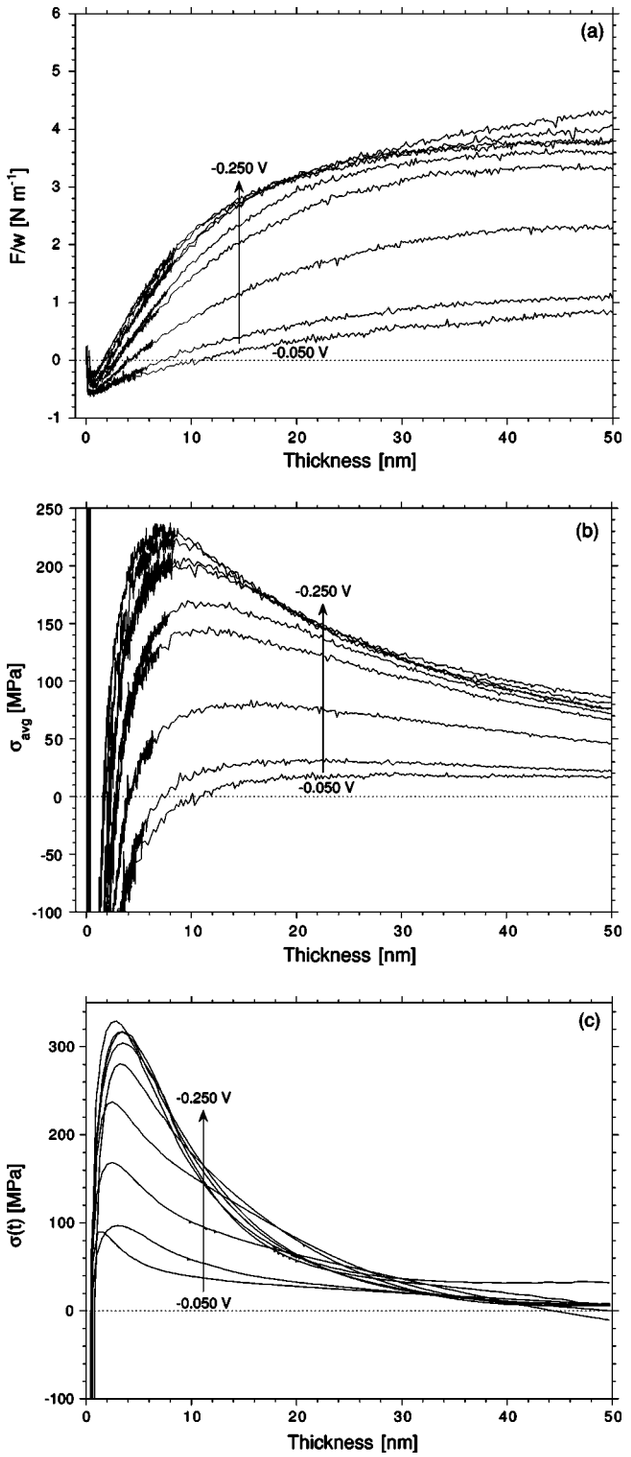

Figure 5. (a) Force per cantilever beam width, F/w, (b) the average film stress, σ_{avg}, and (c) the incremental film stress, $\sigma(t)$, plotted as a function of deposit thickness (up to 50 nm) for copper deposited onto (111)-textured Au in 0.1 mol L^{-1} H_2SO_4 + 10 mmol L^{-1} $CuSO_4$, as a function of deposition potential. The potential was stepped from +0.3 V to a deposition potential ranging from −0.05 to −0.25 V in 0.025 V increments.

initial deflection (see Fig. 5a) is tensile (from 0 N m^{-1} to about 0.2 N m^{-1}) and then compressive (to about −0.5 N m^{-1}) which reflects the two steps of the Cu upd process. The cantilever then moves in the tensile direction, the rate of which is a function of the deposition potential. Figure 5b shows the average in-plane stress associated with the bulk deposition of copper for a thickness up to 50 nm. For all deposition potentials examined, the average film stress is tensile and reaches a maximum value in the first 10 nm at the more cathodic overpotentials. The magnitude of the maximum average tensile stress as well as the film thickness at which the maximum occurs are both dependent upon the electrode potential. This rapid tensile rise and its dependence on deposition potential are consistent with nuclei coalescence and grain boundary formation. Similar results have been reported by Haiss[29] for the earliest stages of copper deposition (25 monolayers). Figure 5c shows the incremental stress which is simply the slope of the F/w-thickness curves in Fig. 5a. These curves have the same general shape as the average film stress but clearly indicate that the growth processes responsible for the tensile stress are only active during the earliest stages of deposition. The maximum incremental stresses are observed in the first 2 to 3 nm of deposition but there does not appear to be a clear relationship between the thickness at which the maximum incremental stress occurs and the potential. This may be an indication that the polynomials used to fit the beam deflection data in Fig. 5a may not have properly captured the inflection point. However, the incremental stress data does indicate that although the films still have an average tensile stress when they reach a thickness of 30 nm, the Cu that is deposited beyond that point is nearly stress-free.

A summary of the maximum average and incremental stresses and their dependence on deposition potential is shown in Fig. 6. In addition to the film stress, an estimate of the nucleation density at each potential was calculated from the current maxima in Fig. 4 using the appropriate expression for instantaneous three-dimensional nucleation followed by diffusion controlled growth[55]

$$N_o = 0.065\left(\frac{1}{8\pi C_o V_m}\right)^{1/2}\left(\frac{nFC_o}{i_{max}t_{max}}\right)^2 \quad [7]$$

where N_o is the nucleation density, C_o is the bulk concentration of Cu^{2+} in the electrolyte, V_m is the molar volume for copper, i_{max} and t_{max} are the magnitude and time of the current maximum, respectively, and the remaining symbols have their usual meaning. Figure 6 indicates that as the deposition potential is made more negative, the nucleation density increases while both the maximum average and incremental film stress increases. This is a clear indication that the tensile stress developed in the early stages of copper deposition is linked to the grain boundary density of the deposit.

Tensile stress generated during film growth is an indication that the density of the film is increasing while the film is constrained by the substrate. The formation of small-angle grain boundaries as the result of nuclei coalescence and recrystallization (or the general elimination of defects in the film) are two processes that can account for this. It is clear from Fig. 5 that the tensile contribution to the stress occurs when the charge-equivalent of a few monolayers of Cu has been deposited. This is somewhat faster than one would expect from coalescence of a random distribution of nuclei. Haiss also observed this early tensile transition and attributed it to preferred nucleation at step edges and surface defect sites.[29] Nichols has shown by *in situ* STM that Cu nano-crystallites, nucleated at steps, start to coalesce after just one or two monolayers of bulk Cu have been deposited.[56]

Estimates of the maximum tensile stress associated with nuclei coalescence for high-mobility Volmer-Weber growth can be found in the physical vapor deposition (pvd) literature[3,57,58]

$$\sigma_{max} = \frac{2\Delta\gamma}{R_I} \quad [8]$$

where $\Delta\gamma$ is the energy recovered by converting two free surfaces into a grain boundary ($\approx$2 J m^{-2}) and R_I is the nuclei radius at impingement. Based on Eq. 8 and the maximum stress levels observed in Fig. 5b, the nuclei should have radii on the order of 15 to

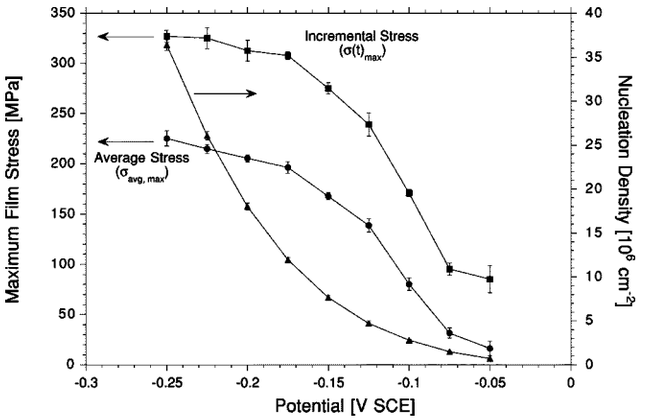

Figure 6. Maximum average and incremental film stresses and transient-derived nucleation density as a function of deposition potential for Cu deposition onto (111)-textured Au in 0.1 mol L^{-1} H_2SO_4 + 10 mmol L^{-1} $CuSO_4$.

250 nm to produce these stresses by coalescence alone. This is significantly smaller than the 2 to 7 μm grain size that one can calculate from the nucleation densities shown in Fig. 6, assuming the nuclei have a hemispherical shape. This may be evidence that the nucleation densities obtained from treating the interacting diffusion fields of the nuclei may be significantly underestimating the actual nucleation density. Grujicic has shown using atomic force microscopy that the measured nucleation densities for copper deposition from sulfate-based electrolytes are typically an order of magnitude higher than those calculated from the current transients.[59]

Early stress models have suggested that coalescence-induced tensile stresses are produced only when the initial coalescence occurs. However, a more recent model by Rajamani *et al.*[60] suggests that stress evolution is an inherent part of the growth process when two neighboring surfaces grow together to form a grain boundary. The stress increases to its maximum value, σ_{max}, as the ratio of the grain boundary length, b, and the height of the grain, h, approaches unity. It seems realistic to imagine b/h increasing due to preferential deposition into the grain boundary, either as the result of direct deposition or the movement of ad-atoms on the surface, as the material that is added to the boundary reduces the elastic strain associated with bringing the surfaces together. An important distinction of this

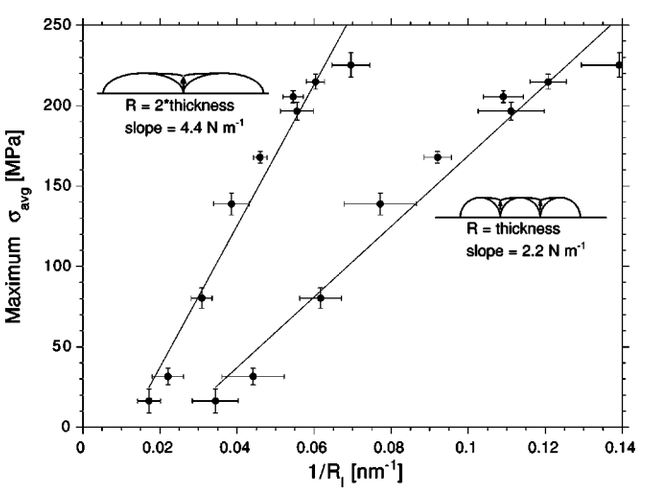

Figure 7. Maximum average film stress as a function of reciprocal nuclei size for Cu deposition onto (111)-textured Au in 0.1 mol L^{-1} H_2SO_4 + 10 mmol L^{-1} $CuSO_4$.

model is that the maximum tensile stress does nor occur at coalescence but when the grain boundary is fully formed, approaching the thickness of the film. Based on this assumption, we can estimate the average radius of the impinging nuclei from the nominal deposit thickness at the tensile maximum, plot σ_{max} *vs.* R_I^{-1}, and compare to Eq. 8. Figure 7 shows two plots using the average stress-thickness data of Fig. 5b. One plot assumes that the nuclei at the point of coalescence have a hemispherical shape so that R_I is the nominal deposit thickness. The second assumes that the nuclei are laterally extended so that R_I is twice the deposit thickness. This second case has some experimental justification where the lateral growth rate of Cu on Au(111) in the absence of additives is reported to be about 2.5 times that of the vertical growth rate.[56] Both σ_{max} *vs.* R_I^{-1} plots show linear behavior with slopes of 2.2 N m^{-1} and 4.4 N m^{-1} for the two cases. These values are very close to that predicted from Eq. 8 where $2\Delta\gamma = 4.0$ N m^{-1} (J m^{-2}) which strongly supports the conclusion that the tensile stress generated in the first 30 nm of deposition is primarily due to the formation of grain boundaries in the film.

To examine the stress development in thicker films, the F/w, the average film stress and the incremental film stress were recorded for deposits up to 400 nm thick, Fig. 8. As in the previous set of curves, the average film stress (Fig. 8b) reaches a maximum tensile value in the first 20 nm. As the deposit thickens, the average film stress decreases rather quickly and becomes compressive in deposits formed at small deposition overpotentials. Figure 8c shows that the incremental stress becomes compressive at a thickness of 75 nm for all deposits except the two formed at potentials more negative than −0.20 V. It is clear that the growth process that follows nuclei coalescence produces a compressive stress that competes with the initial tensile transient. This tensile-to-compressive transition is typically associated with high-mobility island growth and has been observed in copper deposited from the vapor phase.[4] In the pvd literature, this post-tensile compressive stress has been attributed to the nonequilibrium concentration of mobile ad-atoms on the surface which are driven into the grain boundaries.[3,61] Grain boundaries have been shown to play an important role in the generation of compressive stress because it has been observed that films deposited on polycrystalline substrates become compressive while those same films deposited onto single crystal substrates remain tensile.[61,62] More recently, Friesen has attributed the post-tensile compressive stress to the concentration of atomic scale defects on the surface of the film.[63]

If the deposition flux is interrupted during this final compressive stage, a rapid relaxation of the stress occurs. When the flux is resumed, the compressive stress is re-established as if the interruption had not occurred.[4,61,63] An example of this is shown in Fig. 9 where deposition at two different potentials was periodically interrupted to open circuit (OC) for 15 min. The overall shape of both transients is very similar to those for uninterrupted deposition shown in Fig. 8b. In the case of deposition at −0.075 V there is little relaxation in the early stages of deposition, less than 50 nm. As the deposit thickens, the subsequent interruptions to open circuit result in a stress relaxation in the tensile direction. The inset in Fig. 9 shows the relaxation transient when the −0.075 V deposit is interrupted at a thickness of 200 nm (OC#4). During the 15 min interruption, the stress relaxes from a value of −20 MPa to essentially zero. Chason has modeled the compressive relaxation and has confirmed experimentally for the gas-phase deposition of Ag that the stress relaxes exponentially from its steady-state value. The relaxation time constant was dependent on the film thickness and grain size as well as other parameters.[61]

Friesen has examined the reversible stress changes that have been observed at all stages of Volmer-Weber film growth in evaporated copper.[63] Of particular note was the asymmetry in the relaxation and growth stress-time curves; *i.e.*, the initial rate of stress change during a growth interruption was slower than the initial rate of stress change when growth was resumed. If the reversible insertion of mobile ad-atoms into the grain boundaries is rate-limited by grain boundary diffusion, one would expect the formation and relax-

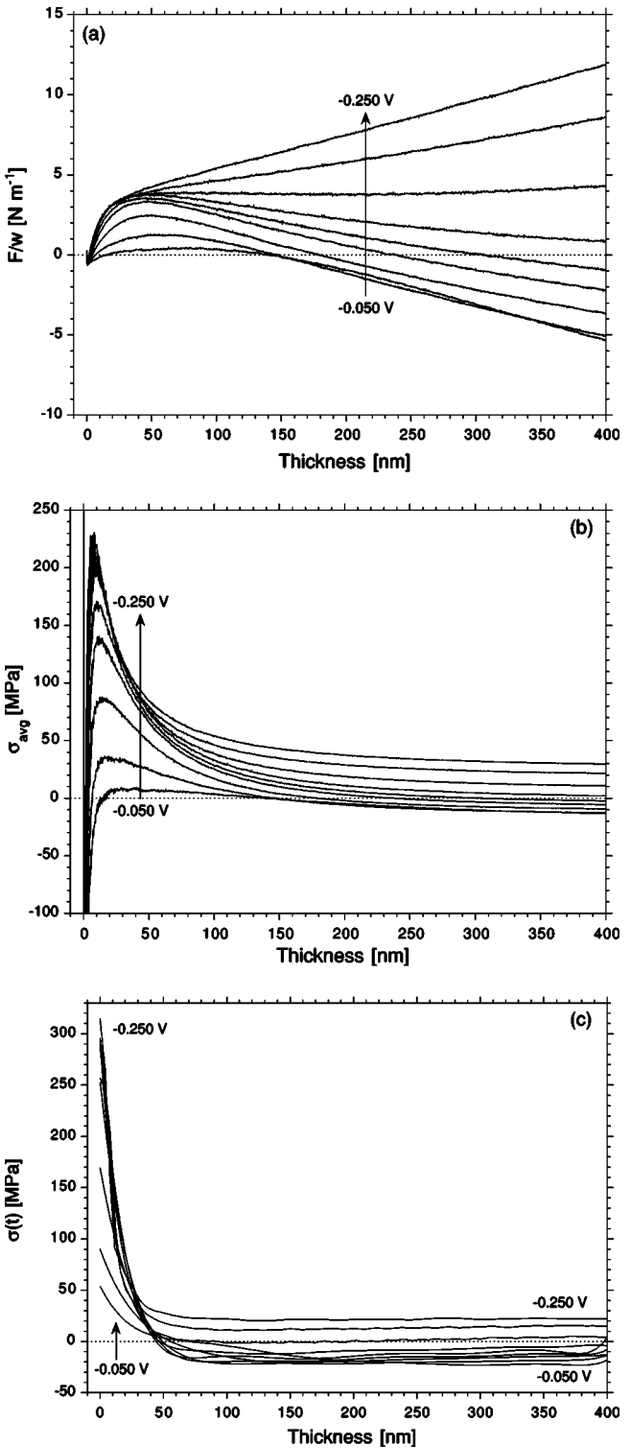

Figure 8. (a) Force per cantilever beam width, F/w, (b) the average film stress, σ_{avg}, and (c) the incremental film stress, $\sigma(t)$, plotted as a function of deposit thickness (up to 400 nm) for copper deposited onto (111)-textured Au in 0.1 mol L^{-1} H_2SO_4 + 10 mmol L^{-1} $CuSO_4$, as a function of deposition potential. The potential was stepped from +0.3 V to a deposition potential ranging from −0.05 to −0.25 V in 0.025 V increments.

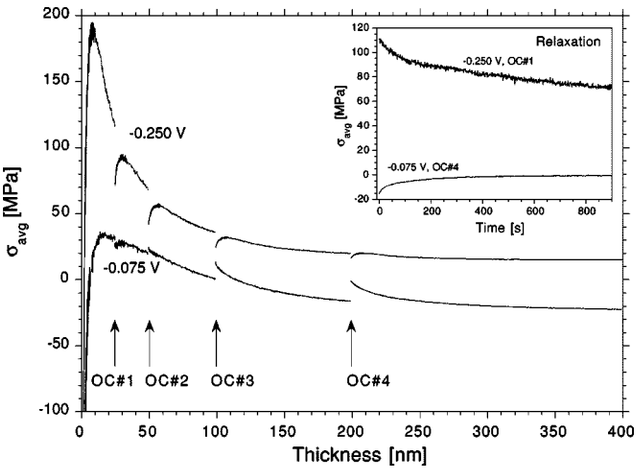

Figure 9. Average film stress in copper deposited onto (111)-textured Au in 0.1 mol L^{-1} H_2SO_4 + 10 mmol L^{-1} $CuSO_4$, as a function of deposit thickness up to 400 nm at deposition potentials of −0.075 and −0.25 V. Deposition was interrupted to open circuit for 15 min at a deposit thickness of 25, 50, 100, and 200 nm. Inset shows stress relaxation for −0.25 V, OC#1 and −0.075 V, OC#4.

ation of the compressive stress to have similar time constants. In addition, Friesen has observed that the magnitude of the reversible stress change is dependent on deposition rate and not deposit thickness. Consequently, their post-tensile compressive stress is attributed to the concentration of atomic scale defects on the surface, the formation and removal of which are not kinetically symmetric.[63] Although we have not fully characterized the relaxation behavior of our electrodeposited copper films, we see a clear dependence of stress relaxation on deposit thickness which suggests that the grain boundaries may in fact have a role in the generation of compressive stresses in the thickening stage of film growth.

Figure 9 also shows that there is significant relaxation of the tensile stress in the early stages of deposition. Similar behavior has been reported for Al deposition from the gas phase.[64] Several mechanisms can account for the tensile stress relaxation including plastic deformation at the interface, intra-granular shear, and surface-Coble creep where surface adatoms diffuse into grain boundaries to relieve the tensile stress created by grain boundary zipping. Because the pzc of Cu is negative of these deposition potentials, sulfate remains (floats) on the Cu surface during deposition. As a consequence, we rule out sulfate adsorption as a mechanism for decreasing the surface stress at open circuit. Interestingly, when deposition is resumed, a smaller, secondary tensile peak appears. This is presumably due to the creation of the final grain boundaries from the original nuclei or perhaps the result of secondary nucleation on the Cu surface brought about by the new potential pulse. Both the tensile relaxation and the subsequent tensile peak diminish as the deposit thickens. This relaxation behavior will be addressed in more detail in subsequent papers.

Conclusions

In situ stress measurements were made on a HeNe optical bench during copper electrodeposition using the wafer curvature method. As the potential of the Au electrode is swept cathodically from +800 mV, the surface stress increases approximately 1.8 N m^{-1} as the sulfate adlayer is removed from the Au surface and replaced by a sulfate-copper honeycomb structure. The completion of the Cu monolayer, which includes the readsorption of sulfate onto the Cu surface, causes a 1 N m^{-1} compressive shift in the surface stress. Within the first 20 nm of bulk Cu deposition, there is a rapid increase in tensile stress that we attribute to nuclei coalescence and grain boundary formation. When the films are continuous, they become compressive. This is consistent with models in the literature describing a non-equilibrium concentration of mobile adatoms on the surface which are driven into the grain boundaries. In the continuous film, the total stress is the superposition of both stress

mechanisms and each has a potential dependence. When deposition is interrupted, both tensile and compressive components of the stress relax but are quickly reestablished when deposition is resumed. The development of the growth stress that we describe here is very similar to that which has been reported for Cu deposition from the vapor phase.

The National Institute of Standards and Technology assisted in meeting the publication costs of this article.

References

1. R. Weil, *Plating*, **58**, 137 (1971).
2. R. Koch, *J. Phys.: Condens. Matter*, **6**, 9519 (1994).
3. J. A. Floro, E. Chason, R. C. Cammarata, and D. J. Srolovitz, *MRS Bull.*, **27**, 19 (2002).
4. A. L. Shull and F. Spaepen, *J. Appl. Phys.*, **80**, 6243 (1996).
5. W. D. Nix and B. M. Clemens, *J. Mater. Res.*, **14**, 3467 (1999).
6. R. Abermann, *Vacuum*, **41**, 1279 (1990).
7. R. Weil, *Plating*, **57**, 1231 (1970).
8. R. Weil, *Plating*, **58**, 50 (1971).
9. M. A. Butler and D. S. Ginley, *J. Electrochem. Soc.*, **134**, 510 (1987).
10. L. Jaeckel, G. Lang, and K. E. Heusler, *Electrochim. Acta*, **39**, 1031 (1994).
11. H. Ibach, *J. Vac. Sci. Technol. A*, **12**, 2240 (1994).
12. J. Scarminio, S. N. Sahu, and F. Decker, *J. Phys. E*, **22**, 755 (1989).
13. J. M. Rosolen and F. Decker, *J. Electrochem. Soc.*, **143**, 2417 (1996).
14. G. G. Lang and M. Seo, *J. Electroanal. Chem.*, **490**, 98 (2000).
15. K. Y. Chung and K.-B. Kim, *J. Electrochem. Soc.*, **149**, A79 (2002).
16. M. Seo and Y. Serizawa, *J. Electrochem. Soc.*, **150**, E472 (2003).
17. W. Haiss and J. K. Sass, *J. Electroanal. Chem.*, **386**, 267 (1995).
18. R. Raiteri and H.-J. Butt, *J. Phys. Chem.*, **99**, 15728 (1995).
19. T. A. Brunt, T. Rayment, S. J. O'Shea, and M. E. Welland, *Langmuir*, **12**, 5942 (1996).
20. T. A. Brunt, E. D. Chabala, T. Rayment, S. J. O'Shea, and M. E. Welland, *J. Chem. Soc., Faraday Trans.*, **92**, 3807 (1996).
21. H. Ibach, *Surf. Sci. Rep.*, **29**, 195 (1997).
22. W. Haiss, R. J. Nichols, J. K. Sass, and K. P. Charle, *J. Electroanal. Chem.*, **452**, 199 (1998).
23. W. Haiss, *Rep. Prog. Phys.*, **64**, 591 (2001).
24. W. Haiss and J. K. Sass, *Langmuir*, **12**, 4311 (1996).
25. W. Haiss and J. K. Sass, *J. Electroanal. Chem.*, **410**, 119 (1996).
26. C. Friesen, N. Dimitrov, R. C. Cammarata, and K. Sieradzki, *Langmuir*, **17**, 807 (2001).
27. S. N. Sahu, J. Scarminio, and F. Decker, *J. Electrochem. Soc.*, **137**, 1150 (1990).
28. H. Feigenbaum and R. Weil, *J. Electrochem. Soc.*, **126**, 2085 (1979).
29. W. Haiss, R. J. Nichols, and J. K. Sass, *Surf. Sci.*, **388**, 141 (1997).
30. G. G. Stoney, *Proc. R. Soc. London, Ser. A*, **82**, 172 (1909).
31. G. Moulard, G. Contoux, G. Motyl, G. Gardet, and M. Courbon, *J. Vac. Sci. Technol. A*, **16**, 736 (1998).
32. Y. Nakai, M. S. Zei, D. M. Kolb, and G. Lehmpfuhl, *Ber. Bunsenges. Phys. Chem.*, **88**, 340 (1984).
33. D. M. Kolb, *Z. Phys. Chem., Neue Folge*, **154**, 179 (1987).
34. M. S. Zei, G. Qiao, G. Lehmpfuhl, and D. M. Kolb, *Ber. Bunsenges. Phys. Chem.*, **91**, 349 (1987).
35. L. Blum, H. D. Abruna, J. White, J. G. Gordon II, G. L. Borges, M. G. Samant, and O. R. Melroy, *J. Chem. Phys.*, **85**, 6732 (1986).
36. O. R. Melroy, M. G. Samant, G. L. Borges, J. G. Gordon II, L. Blum, J. White, M. J. Albarelli, M. McMillan, and H. D. Abruna, *Langmuir*, **4**, 728 (1988).
37. A. Tadjeddine, D. Guay, M. Ladouceru, and G. Tourillon, *Phys. Rev. Lett.*, **66**, 2235 (1991).
38. O. M. Magnussen, J. Hotlos, R. J. Nichols, D. M. Kolb, and R. J. Behm, *Phys. Rev. Lett.*, **64**, 2929 (1990).
39. T. Hachiya, H. Honbo, and K. Itaya, *J. Electroanal. Chem.*, **315**, 275 (1991).
40. S. Manne, P. K. Hansma, J. Massie, B. V. Elings, and A. A. Gewirth, *Science*, **251**, 183 (1991).
41. D. B. Parry, M. G. Samant, H. Seki, M. R. Philpott, and K. Ashley, *Langmuir*, **9**, 1878 (1993).
42. M. F. Toney, J. N. Howard, J. Richer, G. L. Borges, J. G. Gordon, O. R. Melroy, D. Yee, and L. B. Sorenson, *Phys. Rev. Lett.*, **75**, 4472 (1995).
43. M. Nakamura and M. Ito, http://www.spring8.or.jp/e/publication/res_fro/RF01B-02A/061-063.pdf
44. M. R. Deakin and O. R. Melroy, *J. Electroanal. Chem.*, **239**, 321 (1988).
45. G. L. Borges, K. K. Kanazawa, J. G. Gordon II, K. Ashley, and J. Richer, *J. Electroanal. Chem.*, **364**, 281 (1994).
46. J. G. Gordon, O. R. Melroy, and M. F. Toney, *Electrochim. Acta*, **40**, 3 (1995).
47. I. H. Omar, H. J. Pauling, and K. Juttner, *J. Electrochem. Soc.*, **140**, 2187 (1993).
48. Z. Shi and J. Lipkowski, *J. Electroanal. Chem.*, **364**, 289 (1994).
49. Z. Shi and J. Lipkowski, *J. Electroanal. Chem.*, **365**, 303 (1994).
50. Z. Shi, S. Wu, and K. Lipkowski, *Electrochim. Acta*, **40**, 9 (1995).
51. O. M. Magnussen, J. Haengeboeck, J. Hotlos, and R. J. Behm, *Faraday Discuss.*, **94**, 329 (1992).
52. G. J. Edens, X. P. Gao, and M. J. Weaver, *J. Electroanal. Chem.*, **375**, 357 (1994).
53. V. Fiorentini, M. Methfessel, and M. Scheffler, *Phys. Rev. Lett.*, **71**, 1051 (1993).
54. J. Lecoeur and J. B. Bellier, *Electrochim. Acta*, **30**, 1027 (1985).
55. B. Scharifker and G. Hills, *Electrochim. Acta*, **28**, 879 (1983).
56. R. J. Nichols, W. Beckmann, H. Meyer, N. Batina, and D. M. Kolb, *J. Electroanal. Chem.*, **330**, 381 (1992).
57. S. C. Seel, C. V. Thompson, S. J. Hearne, and J. A. Floro, *J. Appl. Phys.*, **88**, 7079 (2000).
58. L. B. Freund and E. Chason, *J. Appl. Phys.*, **89**, 4866 (2001).
59. D. Grujicic and B. Pesic, *Electrochim. Acta*, **47**, 2901 (2002).
60. A. Rajamani, B. W. Sheldon, E. Chason, and A. F. Bower, *Appl. Phys. Lett.*, **81**, 1204 (2002).
61. E. Chason, B. W. Sheldon, L. B. Freund, J. A. Floro, and S. J. Hearne, *Phys. Rev. Lett.*, **88**, 156103 (2002).
62. V. Ramaswamy, Ph.D. Thesis, Stanford University (2000).
63. C. Friesen, S. C. Seel, and C. V. Thompson, *J. Appl. Phys.*, **95**, 1011 (2004).
64. J. A. Floro, S. J. Hearne, J. A. Hunter, P. Kotula, E. Chason, S. C. Seel, and C. V. Thompson, *J. Appl. Phys.*, **89**, 4886 (2001).